Geochimica et Cosmochimica Acta 394 (2025) 182–193

Contents lists available at ScienceDirect

Geochimica et Cosmochimica Acta

journal homepage: www.elsevier.com/locate/gca

The redox dependence of the fluid/melt partitioning of tin

Hans Keppler *, Andreas Audétat

Bayerisches Geoinstitut, University of Bayreuth, 95440 Bayreuth, Germany

ARTICLE INFO

Associate editor: Zoltan Zajacz

Keywords:
Tin
Partitioning
Salinity
Hydrothermal deposits
Oxygen fugacity
Redox

ABSTRACT

The partitioning of Sn between a mildly peraluminous granitic melt and saline aqueous fluids was studied at 800 °C and 150 MPa for oxygen fugacities ranging from the Fe-FeO to the Fe_3O_4-Fe_2O_3 buffer. Experiments were carried out in rapid-quench cold-seal pressure vessels using water as pressure medium. Oxygen fugacity was buffered by double capsules, except for oxygen fugacities about 0.5 to 1 log units above the Ni-NiO buffer, which correspond to the intrinsic redox conditions imposed by the Ni alloy vessel in contact with water. Run durations were 3–7 days. Fluid/melt partition coefficients were determined by analyzing fluid inclusions and neighboring quenched glass compositions by laser-ablation ICP-MS, assuming that they represent local equilibrium. At all redox conditions studied, the fluid/melt partition coefficient increases roughly linearly with salinity. The highest partition coefficients are observed 0.5 to 1 log units above the Ni-NiO buffer, where $D_{Sn}^{fluid/melt} = 22.8$ is reached for a salinity of 25 eq. % NaCl in the fluid. Towards more oxidizing conditions (Re-ReO_2 and Fe_3O_4-Fe_2O_3 buffer), the partition coefficient decreases, by about a factor of five for the Fe_3O_4-Fe_2O_3 buffer. This probably reflects the transition from the fluid-soluble Sn^{2+} to the less soluble Sn^{4+}. However, at redox conditions that are more reducing than Ni-NiO, $D_{Sn}^{fluid/melt}$ also strongly decreases. This may be due to the increasing abundance of non-polar H_2 in the fluid, which reduces solvation of polar species. Moderately reducing conditions near the Ni-NiO buffer are therefore optimal for extracting tin out of a residual melt, as they correspond to a maximum in the fluid/melt partition coefficient. However, the association of hydrothermal tin deposits with reduced granites is likely also due to the effect of oxygen fugacity on the partitioning of tin between minerals and silicate melt. Indeed, observations made in the course of this study suggest that the solubility of cassiterite SnO_2 in silicate melts under oxidizing conditions (Fe_3O_4-Fe_2O_3 buffer) is even much lower than previously thought. Overall, the results show that tin extraction by magmatic fluids is rather inefficient and tin enrichment requires extensive fractional crystallization. A *relatively* efficient way to extract tin out of a granitic magma may be fluid release by decompression due to the formation of fractures followed by rapid crystallization induced by water-loss from the melt.

1. Introduction

Tin is one of the oldest metals used by humans; in modern technology, there is an increasing demand for tin in electronics for lead-free solders. Historically, Cornwall (possibly the “tin islands” of Roman age) and the Erzgebirge have been important mining sites in Europe up to recent times (e.g. Breiter, 2012; Simons et al., 2017; Korges et al., 2018) while most of the current production is located in Southern China and the Southeast Asian tin belt (Schwartz et al., 1995; Lehmann, 2021). A large part of the present tin production comes from secondary, placer-type deposits, but the primary tin deposits are almost always related to granites. Typically, porphyry tin, vein, or tin greisen type deposits (Heinrich, 1990; Launay et al., 2019) are associated with highly fractionated, peraluminous, S-type granites (e.g. Lehmann, 1990; Simons et al., 2017).

Tin-bearing granites are typically generated by anatexis of sedimentary (often pelitic) precursors, with or without significant pre-enrichment (Lehmann, 1990; Romer and Kroner, 2016; Wolf et al., 2018). Economic grade tin concentrations are apparently the result of a combination of fractional crystallization and – possibly – preferential partitioning of tin into a fluid phase at the very end of magma evolution (Heinrich, 1990; Lehmann, 1990, 2021). Fractional crystallization alone may enrich tin to the level of 1000–2000 ppm in residual silicate melts (Webster et al., 1997). A strong enrichment of fluorine and boron is also often observed in these melts, and a prevalence of either F or B has been associated with different styles of mineralization (Pollard et al., 1987).

* Corresponding author.
E-mail address: hans.keppler@uni-bayreuth.de (H. Keppler).

https://doi.org/10.1016/j.gca.2025.02.007
Received 9 September 2024; Accepted 4 February 2025
Available online 5 February 2025

Boron may already have been pre-enriched in the marine sediments that were the precursors of the S-type granites (Lehmann, 1990).

Already Ishihara (1977) noted the importance of oxygen fugacity for the enrichment of tin (see also Ishihara, 1981; Lehmann, 1982; Lehmann, 1990). Cassiterite SnO_2 with Sn in the + 4 oxidation state is the only economically important mineral of tin. However, in addition to the + 4 oxidation state, the + 2 state of Sn is also relatively stable and in general, compounds of Sn^{2+} are much more water-soluble than those of Sn^{4+}. It is therefore plausible that reducing conditions may enhance the mobility of tin during ore-forming processes. Indeed, as noted by Lehmann (1990), tin-bearing granites appear to be generally much more reduced than granites with porphyry copper or porphyry molybdenum mineralization.

Experimental studies in haplogranitic systems (Linnen et al., 1995, 1996; Bhalla et al., 2005) show an increase of cassiterite solubility by orders of magnitude with decreasing oxygen fugacity. Under the most reducing conditions studied, tin solubilities of several wt. % in the melt are reached. In a log Sn versus log fO_2 plot, the data follow nicely a straight line with slope of −0.5, as expected from the reaction

$$SnO_2\,(\text{cassiterite}) = SnO\,(\text{melt}) + 1/2\,O_2$$

Only at rather high oxygen fugacities – more than one log unit above the Ni-NiO buffer – cassiterite solubility appears to become independent of fO_2 because at these redox conditions, SnO_2 may dissolve as Sn^{4+} in the melt, which does not involve any change in oxidation state. XAFS measurements of quenched Sn-bearing glasses further suggest that the Sn^{2+}/Sn^{4+} ratio is a strong function of melt composition (Farges et al., 2006). The strong effect of oxygen fugacity on tin solubility in silicate melt is also seen in mineral/melt partitioning data. Wei et al. (2024) observed that tin is generally highly incompatible in most minerals under reducing conditions, but becomes compatible in biotite, clinopyroxene, titanomagnetite and spinel at high oxygen fugacity.

High-pressure experiments with tin-bearing samples, in particular those at low oxygen fugacity, suffer from the problem of tin alloying with the noble metals (Au or Pt) of the sample capsule. Early studies on tin solubility in fluids and on the fluid/melt partitioning of tin have been hampered by alloying problems and losses of tin from the charge. Both Nekrasov et al. (1980) and Keppler and Wyllie (1991) observed that the presence of Cl enhances the partitioning of Sn into the fluid; however, the measured partition coefficients remained low ($D_{Sn}^{fluid/melt}$ from 0.0008 to 0.078, 750 °C, 2 kbar, Ni-NiO buffer; Keppler and Wyllie, 1991), such that a significant tin transport by fluids would not be expected. A clear effect of fluorine on the partitioning of tin between melt and fluid was not observed. A more recent study by Hu et al. (2008) was carried out at 1 kbar and 850 °C close to the Ni-NiO buffer. They confirmed that in the absence of Cl, $D_{Sn}^{fluid/melt}$ is rather low, but increases with HCl concentration, while HF has little effect. However, the absolute values of measured partition coefficients are higher than in previous studies; they range from 0.13 to 4.43 in the absence of Cl, and for 2 M and 4 M HCl solutions, even partition coefficients up to 53.6 are reported. However, it is concerning that in the study of Hu et al. (2008), possible problems of Sn alloying with the gold capsules were not considered. The authors argued that due to the low bulk tin contents in their charges, this effect may not be important. Moreover, to determine fluid compositions, they washed the inside of the capsules after the experiments with dilute nitric acid and combined this solution with that withdrawn from the capsule after the experiments. It is easy to see that by using this procedure, some tin adsorbed on the surface of the gold capsule may have been re-dissolved, leading to erroneously high fluid concentrations and fluid/melt partition coefficients of tin.

Different strategies have been proposed to overcome the problems with tin loss to noble capsules that had plagued early experiments. Duc-Tin et al. (2007) developed a method to study cassiterite solubility in aqueous fluids by trapping cassiterite crystals together with fluid in synthetic fluid inclusions. After equilibration, which occurred in a fluid sample that was completely enclosed in quartz, the fluid inclusions often "necked down" into inclusions with cassiterite and inclusions containing only fluid. By laser-ablation of fluid-only inclusions, the solubility of cassiterite could therefore be accurately measured. By combining these data on the solubility of SnO_2 in aqueous fluids with the data on cassiterite solubility in silicate melts under similar conditions, Duc-Tin et al. (2007) estimated the fluid/melt partition coefficient $D^{fluid/melt}$ of Sn near the Ni-NiO buffer to be 0.1–0.5 for metaluminous melts in equilibrium with moderately saline (5 wt% NaCl + KCl) fluids at 700 °C and 100–200 MPa. For peraluminous melts, the predicted $D^{fluid/melt}$ would be between 2 and 4. More recently, Zhao et al. (2022) developed an elegant approach for measuring $D^{fluid/melt}$ of Sn, which appears to completely solve the problem of tin loss to noble metal capsules. They showed that the laser ablation analysis of fluid inclusions in quenched glasses and of the neighboring glass itself appear to preserve the local equilibrium distribution of Sn between melt and fluid before quenching. Even if some tin is continuously lost to the capsule wall during the experiment, equilibrium fluid/melt partition coefficients can still be measured with this approach. Zhao et al. (2022) measured the partitioning of Sn between granitic melt and aqueous fluid as a function of salinity and ASI (aluminum saturation index), but at a constant oxygen fugacity near the Ni-NiO buffer. In the current study, we use experimental methods similar to those of Zhao et al. (2022) to investigate the dependence of the fluid/melt partitioning on redox state, as this was often considered to be a major factor in the enrichment of tin to economic ore deposits (e.g. Lehmann, 2021).

2. Methods

2.1. Starting materials and sample preparation

Starting materials for the experiments were synthetic, Sn-bearing granitic glasses and solutions of NaCl + KCl in water. Two glasses with different Sn content (about 1000 and 100 ppm) were prepared (see Table 1); otherwise, the composition of the glasses was very similar to those used by Zhao et al. (2022). Glasses were prepared in alumina (Al_2O_3) crucibles to avoid any tin loss due to alloying with platinum. High-purity SiO_2, $Al(OH)_3$, Na_2CO_3, K_2CO_3, Fe_2O_3, and SnO_2 were mixed in stoichiometric proportions and ground up in a agate mortar under ethanol. After drying, the mixture was slowly heated in an alumina crucible over 12 h to 1100 °C and kept at this temperature for another 12 h to de-carbonate and de-hydrate. The sample with the crucible was then transferred to a high-temperature furnace, melted at 1600 °C for one hour and then quenched to a glass by dropping the crucible in distilled water. The crucible was destroyed by this procedure. Fragments of the glass were collected and pieces that had been in direct contact with the alumina were discarded. The separated glass was then ground in an agate mortar under ethanol and dried. Saline solutions were prepared by dissolving adequate amounts of high-purity NaCl and KCl in water. Solutions were prepared with a molar ratio of Na:K of 1 and

Table 1
Composition of starting materials (in wt. %).

	High Sn glass	Low Sn glass
SiO_2	73.6 (13)	78.1 (21)
Al_2O_3	13.96 (88)	11.3 (13)
FeO	0.70 (12)	0.71 (9)
Na_2O	3.85 (23)	3.27 (42)
K_2O	5.26 (13)	4.70 (29)
SnO_2	0.15 (7)	< DL
Sum	97.6 (4)	98.1 (5)
ASI	1.16	1.08

Compositions were determined by electron microprobe as averages of about 15 measurement points. Numbers in parentheses are one standard deviation in the last digit. ASI is the alumina saturation index, $Al_2O_3/(Na_2O + K_2O)$ in molar units. < DL = below detection limit; the nominal tin concentration in this sample is 100 ppm Sn or 0.013 wt% SnO_2.

Table 2
Summary of the experimental data on the fluid/melt partitioning of tin at 150 MPa and 800 °C.

Run No	(Na,K)Cl wt.% $NaCl_{eq}$	starting glass	buffer	duration hrs	$D^{fluid/melt}$	n
Sn1	5	high Sn	Ni-NiO + 0.5	94	3.5 (7)	7
Sn2	10	high Sn	Ni-NiO + 0.5	94	7.5 (14)	3
Sn3	15	high Sn	Ni-NiO + 0.5	94	11.5 (45)	5
Sn4	5	high Sn	Co-CoO	96	0.53 (28)	5
Sn5	10	high Sn	Co-CoO	92	1.41 (20)	2
Sn6	15	high Sn	Co-CoO	93	3.59 (118)	3
Sn13	20	high Sn	Ni-NiO + 0.5	187	18.1 (40)	6
Sn14	25	high Sn	Ni-NiO + 0.5	187	22.9 (28)	5
Sn15	20	high Sn	Co-CoO	70	9.2 (21)	5
Sn16	25	high Sn	Co-CoO	96	13.1 (20)	5
Sn17	5	low Sn	Fe_2O_3-Fe_3O_4	96	2.4 (3)	4
Sn19	15	low Sn	Fe_2O_3-Fe_3O_4	96	7.8	1
Sn20	20	low Sn	Fe_2O_3-Fe_3O_4	96	2.9 (8)	6
Sn21	25	low Sn	Fe_2O_3-Fe_3O_4	96	4.3 (12)	5
Sn23	25	high Sn	Fe-FeO	72	7.9 (8)	5
Sn27	5	low Sn	Fe_2O_3-Fe_3O_4	72	<0.9*	6
Sn28	10	low Sn	Fe_2O_3-Fe_3O_4	72	<1.3*	6
Sn29	15	low Sn	Fe_2O_3-Fe_3O_4	72	1.6 (3)	3
Sn30	25	low Sn	Re-ReO_2	90	10.9 (12)	6
Sn31	20	low Sn	Re-ReO_2	90	10.0 (9)	6
Sn32	15	low Sn	Re-ReO_2	90	7.8 (12)	6
Sn33	10	low Sn	Re-ReO_2	89	5.2	1
Sn34	5	low Sn	Re-ReO_2	89	2.2	1

Numbers in parentheses give one standard deviation of $D^{fluid/melt}$ in the last digits; n is the number of fluid inclusions analyzed.

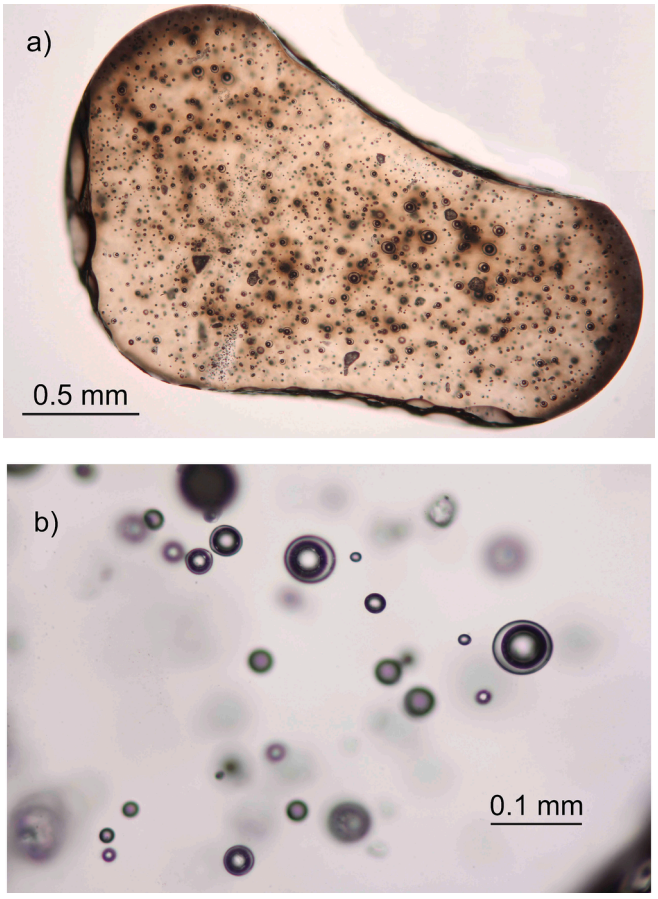

Fig. 1. Images of run products as seen in transmitted light under the microscope. (a) Cross section through the entire sample capsule of experiment Sn30 (Re-ReO_2 buffer) showing numerous inclusions in a brownish glass matrix. (b) Detail of fluid inclusions in sample Sn4 (near Ni-NiO buffer).

with total chloride concentrations (in wt. %) equivalent to 5, 10, 15, 20, and 25 wt% of NaCl in water. These concentrations will be denoted as wt.% $NaCl_{eq}$ in the following text. About 10 mg of solution and 20 mg of granite powder were sealed by arc welding into Au capsules with 3.0 mm outer diameter, 2.7 mm inner diameter, and 20 mm length. Capsules were checked for weight loss by heating in a drying oven to 150 °C. For experiments close to the Ni-NiO buffers, the 3 mm diameter capsules were directly placed into the autoclave and oxygen fugacity was controlled by the intrinsic fO_2 of the pressure vessel. For all other experiments, the 2 mm gold capsules were arc sealed together with 40–50 mg of distilled water and 200–600 mg of a solid buffer (Huebner, 1973) into 30 mm long gold capsules with 5 mm outer diameter and 0.2 mm wall thickness. These capsules were also checked for leaks by drying at 150 °C. Solid buffers used were pure Fe_2O_3, a 1:1 (by weight) mixture of Re and ReO_2, pure Co metal powder, or pure Fe metal powder. The rationale behind this was that diffusion of H_2 through the wall of the outer capsule and exchange with the pressure medium rapidly causes the oxidation of some Co or Fe to CoO or FeO or the reduction of some Fe_2O_3

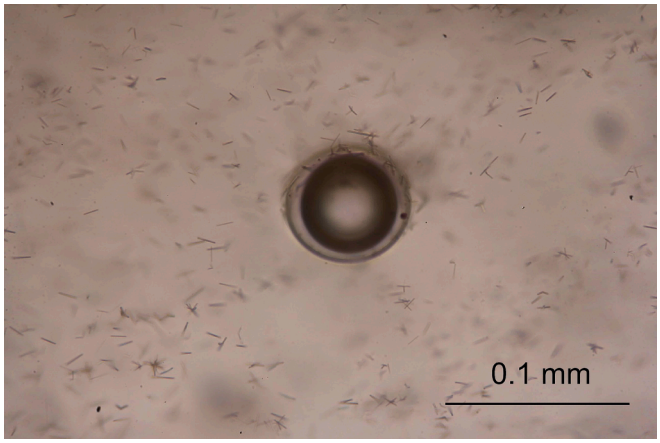

Fig. 2. Transmitted light image of an experimental run product (Sn 9, see Table 4) with the high Sn starting material. Numerous needle-like crystals of cassiterite precipitated in the melt at Fe_2O_3-Fe_3O_4 buffer conditions.

Table 3
Composition of run product glasses (in wt. %).

Run	SiO_2	Al_2O_3	FeO	Na_2O	K_2O	Cl	Sum	ASI
Sn1	71.3 (6)	12.8 (4)	0.43 (10)	3.40 (17)	4.86 (14)	0.099 (28)	92.9 (4)	1.17
Sn2	71.8 (9)	12.8 (5)	0.32 (8)	3.53 (17)	4.92 (14)	0.126 (24)	93.5 (5)	1.15
Sn3	70.7 (12)	13.0 (7)	0.33 (8)	3.70 (21)	4.93 (15)	0.177 (21)	92.9 (5)	1.14
Sn4	71.4 (10)	12.8 (5)	0.31 (8)	3.50 (18)	4.91 (11)	0.082 (24)	93.1 (4)	1.16
Sn5	70.7 (12)	12.7 (7)	0.28 (9)	3.74 (19)	5.03 (16)	0.133 (37)	92.6 (5)	1.09
Sn6	71.0 (8)	12.3 (5)	0.25 (6)	3.73 (13)	4.88 (15)	0.164 (27)	92.4 (3)	1.08
Sn7*	70.7 (8)	13.0 (3)	0.32 (5)	3.50 (9)	4.75 (8)	0.141 (14)	92.5 (6)	1.20
Sn8*	70.7 (10)	13.0 (4)	0.27 (7)	3.68 (15)	4.75 (12)	0.183 (20)	92.6 (7)	1.16
Sn9*	69.1 (11)	13.7 (5)	0.29 (8)	3.90 (14)	4.85 (8)	0.199 (31)	92.1 (6)	1.17
Sn13	69.5 (8)	12.7 (4)	0.13 (5)	3.78 (18)	4.90 (10)	0.186 (30)	91.2 (5)	1.1
Sn14	69.9 (6)	12.7 (4)	0.11 (8)	3.81 (15)	4.87 (12)	0.194 (27)	91.6 (5)	1.1
Sn15	69.6 (8)	12.8 (4)	0.14 (7)	3.97 (17)	4.96 (15)	0.188 (22)	91.7 (3)	1.08
Sn16	69.5 (7)	12.7 (4)	0.19 (6)	3.89 (16)	4.94 (19)	0.204 (54)	91.5 (6)	1.08
Sn17	71.8 (5)	11.6 (2)	0.47 (9)	3.29 (9)	4.64 (10)	0.126 (26)	92.0 (4)	1.11
Sn19	71.6 (13)	11.9 (7)	0.28 (6)	3.58 (26)	4.79 (13)	0.193 (28)	92.4 (3)	1.07
Sn20	70.6 (11)	12.1 (6)	0.30 (9)	3.62 (23)	4.72 (18)	0.215 (45)	91.5 (4)	1.09
Sn21	71.6 (6)	11.8 (4)	0.29 (8)	3.53 (13)	4.66 (12)	0.189 (23)	92.1 (4)	1.09
Sn23	70.5 (8)	12.5 (5)	0.55 (18)	3.72 (17)	5.26 (29)	0.237 (33)	92.7 (7)	1.06
Sn27	72.2 (8)	12.1 (5)	0.48 (10)	3.21 (18)	4.58 (15)	0.069 (20)	92.7 (5)	1.18
Sn28	73.2 (10)	12.0 (5)	0.41 (9)	3.35 (19)	4.66 (14)	0.131 (24)	93.7 (3)	1.13
Sn29	71.7 (13)	12.3 (7)	0.34 (8)	3.54 (23)	4.73 (18)	0.170 (31)	92.8 (5)	1.12
Sn30	71.4 (12)	12.1 (6)	0.12 (8)	3.64 (23)	4.84 (16)	0.179 (32)	92.4 (6)	1.08
Sn31	71.3 (12)	12.4 (6)	0.35 (7)	3.64 (19)	4.73 (14)	0.194 (32)	92.7 (5)	1.12
Sn32	69.3 (11)	11.4 (7)	0.36 (4)	3.92 (27)	4.75 (17)	0.170 (18)	89.9 (5)	0.98
Sn33	68.9 (10)	11.6 (4)	0.35 (3)	3.96 (19)	4.82 (11)	0.155 (15)	89.8 (5)	0.99
Sn34	68.8 (10)	11.8 (6)	0.44 (4)	3.88 (20)	4.83 (12)	0.111 (17)	89.9 (4)	1.01

Compositions were determined by electron microprobe as averages of about 15 measurement points. Numbers in parentheses are one standard deviation in the last digit. ASI is the alumina saturation index, Al_2O_3/ (Na_2O + K_2O) in molar units. Experiments marked with a star (*) are "failed" runs, where needles of cassiterite precipitated from the melt and measuring fluid inclusions was impossible. However, these runs are useful to constrain cassiterite solubility in the melt under oxidizing conditions.

to Fe_3O_4. Indeed, these phases were always detected in the respective buffers after the end of the experiments; excess water was also still present in both the outer and the inner capsule.

2.2. Hydrothermal experiments

All experiments were caried out at 800 °C and 150 MPa in vertical, rapid-quench cold-seal vessels made of the Inconel 713 LC superalloy. The reaction of this Ni-rich alloy with the water used as pressure medium creates an intrinsic oxygen fugacity about 0.5 to 1 log unit above the Ni-NiO buffer (Keppler, 2010; Fang et al., 2024). Samples were attached at the top of a sample holder and kept in the hot spot near the top of the vessel by an external magnet acting on a magnetic piece at the base of the sample holder. Run durations ranged from 2 to 8 days. At the end of a run, the sample was slowly lowered into a water-cooled zone within about 5 min. This relatively slow quench was chosen to avoid the decrepitation of fluid inclusions by thermal shock.

2.3. Investigation of run products

After quenching, sample capsules were cleaned and weighed to detect leaks. First the outer and then the inner capsule were separately pierced with a needle, dried, and weighed to detect the presence of water. The presence of an intact buffering assemblage in the outer capsule was controlled by visible inspection and sometimes by X-ray diffraction. Glass pieces from the inner capsule were embedded in epoxy resin and polished. The major element composition of the quenched glasses was measured by electron microprobe (JEOL SuperProbe JXA-iSP100) at 10 kV, 10 nA using a 10 µm defocused beam. Count times were 20 s on peak and 10 s on background. Standards used were quartz (SiO_2), andalusite (Al_2O_3), hematite (FeO), albite (Na_2O), orthoclase (K_2O), and sodalite (Cl). Na was always measured first to avoid losses. Tin concentrations in fluid inclusions and adjacent glass were measured by laser-ablation ICP-MS using a 193 nm ArF GeolasPro excimer laser (Coherent, USA) attached to an Elan DRC-e quadrupole ICP–MS unit (Perkin Elmer, Canada). Analyzed isotopes comprise ^{23}Na, ^{27}Al, ^{30}Si, ^{35}Cl, ^{39}K, ^{57}Fe, ^{85}Rb, ^{118}Sn, ^{120}Sn and ^{197}Au, using 10–50 ms dwell time. The analyses were performed in a rhombic sample chamber with a volume of ~ 8 cm^3 that was flushed by He gas at a rate of 0.4 l/min, and to which 5 ml/min H_2 was added on the way to the ICP-MS. The ICP-MS was tuned to a ThO/Th oxide production rate of 0.05–0.10 % and a rate of doubly-charged Ca ions of 0.15–0.20 % based on measurements of NIST SRM 610 glass. The analyses of experimental glasses were externally standardized on NIST SRM 610 (Jochum et al., 2011) for Sn, and on rhyolite OA-1 (Wu et al., 2022) for all other elements. Internal standardization was done by normalizing the sum of all element oxides to 95 wt%, assuming a melt water content of 5 wt% at the experimental pressure of 150 MPa (Holtz et al., 1995). For the quantification of the fluid inclusion analyses, glass host was in a first step numerically subtracted from the mixed fluid + glass analyses until no Si was left. The remaining signal was then quantified based on the Cl content of the starting solution as internal standard. Externally standardization was performed on NIST SRM 610, except for Cl, which was standardized on a well-characterized natural afghanite sample. Errors in fluid/melt partition coefficients were calculated by propagating the errors from the fluid and the melt analyses.

Table 4
Data on cassiterite solubility in granitic melt at 800 °C, 150 MPa and the Fe_3O_4-Fe_2O_3 buffer.

Run No	(Na,K)Cl wt.% $NaCl_{eq}$	duration hrs	ASI	Sn ppm by wt.	n
Sn7	5	98	1.20	81 (2)	4
Sn8	10	95	1.16	88 (5)	4
Sn9	15	98	1.17	91 (9)	4

All experiments were carried out with the high Sn starting material and precipitated abundant cassiterite needles during the run. Sn concentrations were measured by laser-ablation ICP-MS on glass between the cassiterite crystals.

3. Results

3.1. Description of run products

A summary of all successful experiments is compiled in Table 2. Run products usually were glasses without crystals, but containing numerous fluid inclusions up to about 50 μm in size (Fig. 1). Glasses produced under reducing conditions were almost colorless, while those from runs at the Re-ReO_2 and Fe_2O_3-Fe_3O_4 buffer had a distinctly brown color due to the presence of ferric iron. Glass compositions are compiled in Table 3. Fluid inclusions were usually two-phase, with a liquid phase and a vapor shrinkage bubble. Only in the runs with highest salinities (25 wt% $NaCl_{eq}$), daughter crystals of salt were sometimes observed. Originally, it was planned to carry out all experiments with the same "high Sn" starting material containing about 1000 ppm of Sn (Table 1). The reasoning here was that allowing for preferential partitioning of tin into the fluid and continuous tin loss due to alloying with the capsule wall, the resulting concentration of Sn in the melt would be below cassiterite saturation even for high oxygen fugacities (Linnen et al., 1995, 1996). Rather surprisingly, however, runs with this starting material at the hematite-magnetite buffer showed the precipitation of cassiterite needles during the experiments with the Sn concentrations in the glass between the needles being as low as 85 ppm (Table 4). For this reason, a second "low Sn" starting material with only about 100 ppm was prepared (Table 1) and used for all experiments at the hematite-magnetite or Re-ReO_2 buffer. The two starting materials are both mildly peraluminous, but with slightly different alumina saturation index (ASI = molar ratio of $Al_2O_3/(Na_2O + K_2O)$). However, after equilibration with the saline fluid, the composition of most run product glasses was rather similar (Table 3), with an average ASI of all successful experiments of 1.09 ± 0.05. In particular, all glasses produced in experiments with the highest fluid salinities fall into a very narrow range of ASI: From 1.08 to 1.12 for 20 wt% $NaCl_{eq}$ and from 1.06 to 1.10 for 25 wt% $NaCl_{eq}$.

While the glasses were usually free of crystals, some of them contained a few small, irregular fragments of corundum, which are probably contamination from the alumina crucibles used for making the starting glasses. An exception were experiments carried out at Fe-FeO buffer conditions, which contained abundant crystals of alkali feldspar inside the glass matrix. The reason for this is likely that at these very reducing conditions, the fraction of H_2 in the fluid phase is about 54 mol %, such that water activity is reduced and the liquidus temperature is raised above the run temperature. Another problem with the high hydrogen contents in the fluid phase was that most of the fluid inclusions produced at Fe-FeO buffer conditions apparently decrepitated or leaked upon pressure release, such that only in one single experiment measurements of the fluid/melt partitioning of tin were possible.

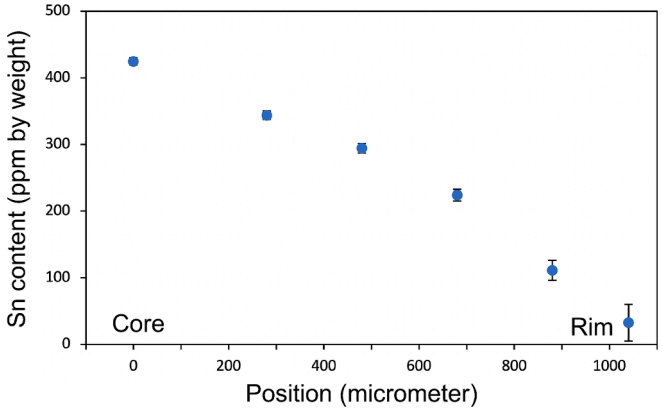

Fig. 3. Tin concentration profile of sample Sn4 from core to rim. During the experiment, tin is continuously being lost by alloying with the Au capsule.

3.2. Fluid/melt partitioning of tin

In all samples, the Sn content of the quenched glasses strongly decreased from the center to the rim (Fig. 3). This is expected, as during the run, tin is continuously lost from the sample by alloying with the gold capsule. The same effect was already described by Zhao et al. (2022). However, despite the one order of magnitude variation in absolute Sn concentration in the glass, analyses of fluid inclusions and of adjacent quenched glass yielded consistent fluid/melt partition coefficients of Sn in all samples studied. As noted by Zhao et al. (2022) this is due to rapid local equilibration despite continuous bulk loss of Sn from the sample. Fig. 4 shows the laser ablation profile of a fluid inclusion with about 80 μm diameter. The elevated signals of Cl, Sn, and Na upon opening of the fluid inclusion by the laser are clearly visible. This requires, however, relatively large fluid inclusions located at relatively shallow distance below the sample surface. For this reason, despite the abundance of small inclusions throughout the sample (Fig. 1 a), in most cases only about five inclusions per sample could be analyzed (Table 2). Analyses of all measured inclusions and of the adjacent glass are compiled in Supplementary Table S1.

Figs. 5 to 7 summarize the measured fluid/melt partition coefficients of tin. In Fig. 5, the data obtained without buffer at the intrinsic oxygen fugacity of the vessel (0.5 to 1 log unit above Ni-NiO) are shown together with the data for the Re-ReO_2 and the Fe_3O_4-Fe_2O_3 buffer. Partition coefficients clearly decrease with increasing oxygen fugacity. This behavior is expected, as compounds of Sn^{2+} are generally much more soluble in water than those of Sn^{4+}. For a constant oxygen fugacity, $D^{fluid/melt}$ of Sn always increases linearly with Cl, indicating the predominance of a Sn species in the fluid with a stoichiometric Cl/Sn ratio of 1, such as SnClOH or $SnCl^+$. The partition coefficients extrapolate to a very small value, probably between zero and one for Cl-free fluids. The data can therefore be described by an equation $D^{fluid/melt} = a\ NaCl_{eq}$, where $D^{fluid/melt}$ is the fluid/melt partition coefficient of Sn and $NaCl_{eq}$ is the equivalent concentration of NaCl in wt. % and a is an empirical constant. Results of linear regression fits of the data are compiled in Table 5. In Fig. 6, Sn partitioning data are shown for oxygen fugacities ranging from the intrinsic value buffered by the vessel (0.5 to 1 log unit above Ni-NiO) to the more reduced conditions of the Co-CoO and Fe-FeO buffers. Very surprisingly, there is no further increase of $D^{fluid/melt}$ of Sn as the system becomes more reducing beyond the Ni-NiO buffer. Rather, $D^{fluid/melt}$ decreases again towards more reducing condition, such that a maximum in $D^{fluid/melt}$ is observed near the Ni-NiO buffer (Fig. 7). This maximum cannot be related to the use of two slightly different starting materials, to differences in ASI or to differences in absolute Sn concentration, for the following reasons: (1) All experimental data shown in Fig. 6 were carried out with the same (high Sn) starting material. In Fig. 5, the series of experiments near the Ni-NiO buffer was carried out with the high Sn starting material, while all runs at both the Re-ReO_2 and Fe_2O_3-Fe_3O_4 buffer were carried out with the low Sn staring material. However, the trend of $D^{fluid/melt}$ with oxygen fugacity is consistent through all three sets of experiments shown in Fig. 5. (2) As noted above, in particular for the experiments with 20 and 25 wt% $NaCl_{eq}$ in the fluid, the values of ASI for all experiments are nearly indistinguishable. (3) Due to the gradients of Sn concentrations in all samples (Fig. 3), the partition coefficients in every run are usually averages of values obtained for variable Sn concentrations, without any obvious concentration dependence of $D^{fluid/melt}$. No such dependence was observed in the study of Zhao et al. (2022) either.

The observed maximum in $D^{fluid/melt}$ cannot be explained by a change in tin oxidation state alone. As long as significant concentrations of both Sn^{2+} and Sn^{4+} coexist in the system, one would normally expect that $D^{fluid/melt}$ increase with decreasing oxygen fugacity, as the abundance of the more fluid-soluble Sn^{2+} increases. This effect likely explains the increase of $D^{fluid/melt}$ from the Fe_2O_3-Fe_3O_4 buffer to near the Ni-NiO buffer. Ultimately, the partition coefficient should then reach a constant value representative of Sn^{2+} alone. Instead, $D^{fluid/melt}$ decreases again

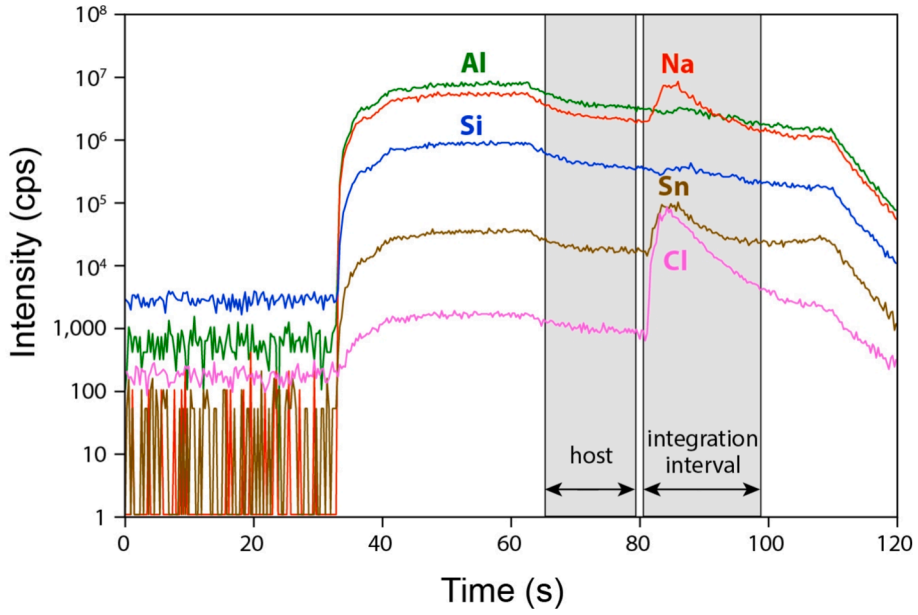

Fig. 4. Laser ablation profile of a 80 μm diameter fluid inclusion in sample Sn6. Upon opening of the fluid inclusion with the laser, the signals of Cl, Sn, and Na sharply increase. The composition of the fluid was determined from the signal within the integration interval, "host" is the signal of the quenched melt that was in equilibrium with the fluid.

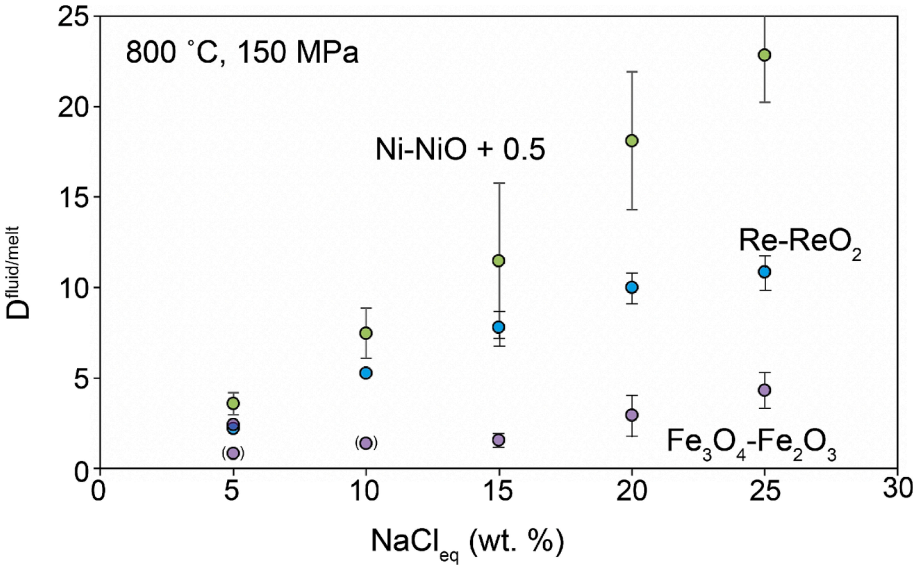

Fig. 5. The fluid/melt partition coefficient of Sn at 800 °C, 150 MPa and oxygen fugacities above the Ni-NiO buffer. Data points in brackets are actually only upper bounds of $D^{fluid/melt}$, as the Sn in the fluid is near or below detection limit. Errors bars shown correspond to one standard deviation.

for oxygen fugacities below Ni-NiO. A possible explanation for this may be that the bulk composition of the fluid changes. While at 800 °C and 150 MPa at an oxygen fugacity 0.5 log units above Ni-NiO, an aqueous fluid consists mostly of H_2O with only a trace (about 0.3 mol %) of H_2, at Fe-FeO buffer conditions, the H_2 content increases to about 54 mol % (as calculated using the thermodynamic data for the Fe-FeO buffer after Huebner, 1973, and data for H_2O vapor after Robie and Hemingway, 1995, assuming ideal mixing between H_2 and H_2O). The replacement of the polar H_2O molecule with its large dipole moment by the non-polar H_2 is expected to reduce the dielectric constant of the fluid. This will also reduce the ability of the fluid to dissolve polar or ionic species and we suggest that this is the main reason why the $D^{fluid/melt}$ of Sn again decreases at oxygen fugacities below the Ni-NiO buffer. Probably, at these reducing conditions, Sn^{2+} is by far the dominant Sn oxidation state both in melt and fluid (Wilson and Eugster, 1990), such that the fluid/melt partition coefficient should normally be insensitive to a further reduction of oxygen fugacity. The observed decrease of D from close to the Ni-NiO to the Fe-FeO buffer conditions may then be due to a change in the solvent properties of the fluid related to increasing H_2.

Unlike the data at all other oxygen fugacities, the results for the Co-CoO buffer in Fig. 6 show a noticeable deviation from a linear trend, which could perhaps indicate the presence of some $SnCl_2$ in the fluid. According to the reaction Sn^{2+} (melt) + $2Cl^-$ (fluid) = $SnCl_2$ (fluid), the ratio of $SnCl_2$ in the fluid to Sn^{2+} in the melt should then increase with the square of the Cl concentration. However, the deviation of the partition coefficients from a linear trend may also still be within experimental uncertainty.

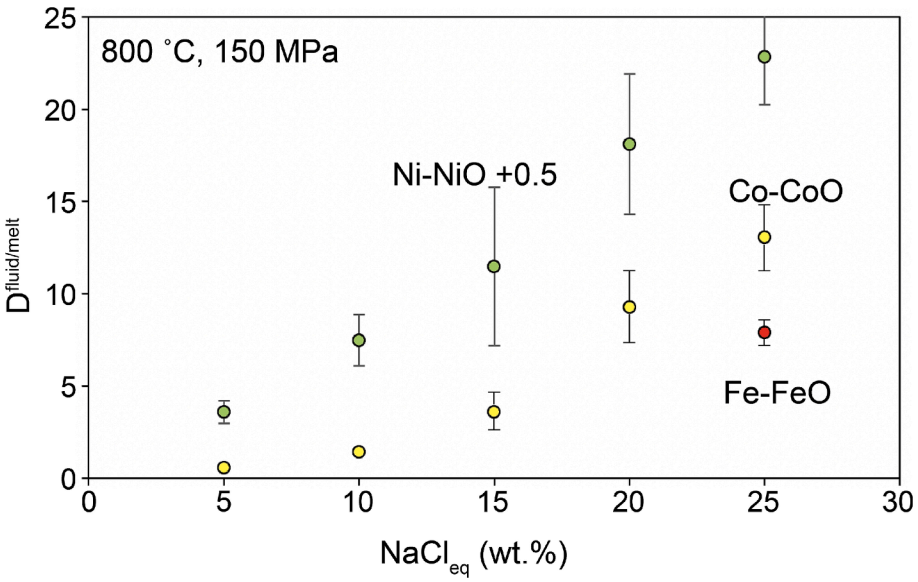

Fig. 6. The fluid/melt partition coefficient of Sn at 800 °C, 150 MPa and oxygen fugacities near and below the Ni-NiO buffer. Errors bars shown correspond to one standard deviation.

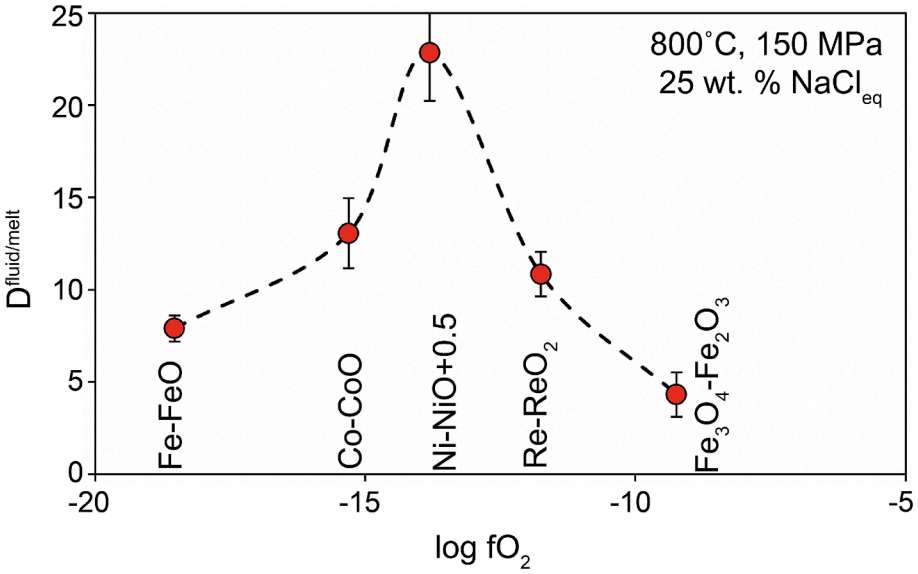

Fig. 7. Fluid/melt partitioning of Sn at 800℃, 150 MPa for a fluid with 25 wt% $NaCl_{eq}$ as a function of oxygen fugacity. Errors bars shown correspond to one standard deviation.

Table 5
Linear regression fits of the fluid/melt partition coefficient of Sn as function of fluid salinity.

Buffer	Coefficient a	R^2
Co-CoO	0.4224	0.9085
Ni-NiO + 0.5	0.8690	0.9940
Re-ReO_2	0.4727	0.9934
Fe_3O_4-Fe_2O_3	0.1571	0.9082

Data at each buffer condition were fitted to an equation $D^{fluid/melt} = a\ NaCl_{eq}$, where $D^{fluid/melt}$ is the fluid/melt partition coefficient of Sn and $NaCl_{eq}$ is the equivalent concentration of NaCl in wt. %. Ni-NiO + 0.5 refers to the intrinsic oxygen fugacity of the autoclave, which is 0.5 to 1 log unit above the Ni-NiO buffer.

4. Discussion

4.1. Comparison with previous studies

Fig. 8 compares the fluid/melt partition coefficient of Sn near the Ni-NiO buffer, as obtained in this study, with data by Zhao et al. (2022) and by Schmidt et al. (2020). All experiments were carried out under similar conditions, i.e. 800 °C, 150 MPa in both this study and in Zhao et al. (2022), and 750 °C, 200 MPa in Schmidt et al. (2020). In all studies, oxygen fugacity was buffered close to Ni-NiO by the intrinsic oxygen fugacity imposed by the Ni alloy vessel in contact with water, and in all studies, fluid compositions were measured by laser-ablation ICP-MS of fluid inclusions. The data by Zhao et al. (2022) overlap with the current results and differences can be explained by differences in the ASI of the studied melt compositions. In particular, those data of Zhao et al. (2022) that fall far below the trend defined by the data of our study in Fig. 8

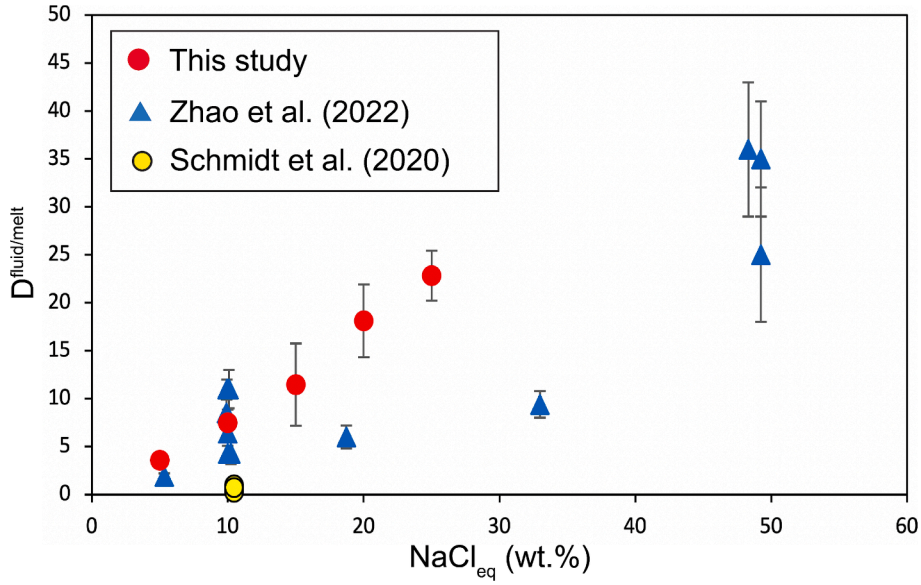

Fig. 8. Comparison of the fluid/melt partition coefficients of Sn near the Ni-NiO buffer measured in this study with those of Zhao et al. (2022) and Schmidt et al. (2020). The pressure–temperature conditions of this study and of Zhao et al. (2022) are identical (800 °C, 150 MPa), those of Schmidt et al. (2020) are similar (750 °C, 200 MPa). Note that the data by Zhao et al. (2022) purposefully cover a much larger range of ASI than those of the current study.

relate to experiments with melts with ASI = 1.05–1.06, significantly below those of our study (1.10–1.17 for runs close to Ni-NiO). A low ASI implies a lower acidity of the fluid (lower ratio of HCl/(Na,K)Cl), which is expected to reduce the solubility of Sn in the fluid (Duc-Tin et al., 2007). Indeed, Zhao et al. (2022) specifically investigated the effect of silicate melt ASI on Sn partitioning at a constant fluid salinity of approximately 10 wt% NaCl equivalent, and their $D^{fluid/melt}$ coincides with our data for an ASI of ~ 1.2, which is not far from the typical values in our study. Compared to both the current work and that of Zhao et al. (2022), the results of Schmidt et al. (2020) appear anomalously low. The reasons for this are not clear; however, it is not obvious whether in the study of Schmidt et al. (2020) glass compositions immediately next to the fluid inclusions were measured to determine $D^{fluid/melt}$. The standardization of the fluid composition to Na could also be a source of error, as suggested by Zhao et al. (2022). Older data obtained by bulk fluid analyses (e.g., Keppler & Wyllie, 1991) are not shown in Fig. 8, as they most likely suffered from tin loss to the capsule walls. We note, however, that the estimate of $D^{fluid/melt}$ of Sn derived by Duc-Tin et al. (2007) from cassiterite solubility experiments agrees very well with the data both of the current study and those of Zhao et al. (2022). For a moderately peraluminous melt composition coexisting with a fluid with 5 wt% $NaCl_{eq}$ salinity at 700 °C, 100—200 MPa and close to Ni-NiO, they predicted $D^{fluid/melt}$ between 2 and 4, in excellent agreement with the direct measurements. For oxygen fugacities significantly above or below the Ni-NiO buffer, we provide here the first data set on the fluid/melt partitioning of tin and there are no published data these results

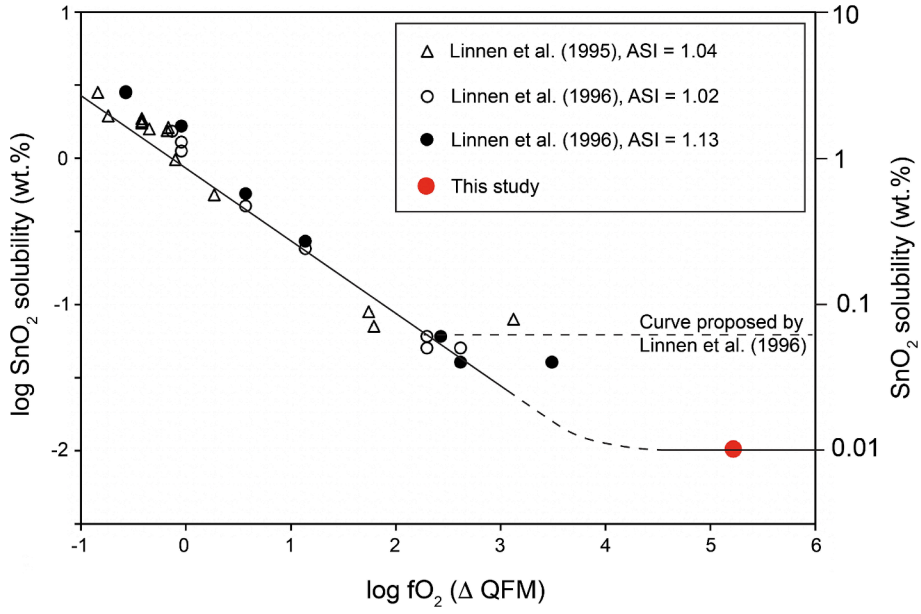

Fig. 9. Cassiterite solubility in granitic melts (800–850 °C, 150–200 MPa) according to Linnen et al. (1995, 1996) and to this study. At high oxygen fugacity, the solubility should become independent of oxygen fugacity, once Sn^{4+} dominates in the melt and the dissolution reaction can be written as SnO_2 (cassiterite) = SnO_2 (melt). Our data suggest that this part of the curve is shifted to lower Sn concentrations than proposed by Linnen et al. (1995, 1996). Note that the red data point actually contains results from three experiments that are nearly identical (Table 4).

could be compared to.

As noted above, one unexpected observation in the course of this study was the precipitation of cassiterite needles in experiments with the "high Sn" starting material at Fe_3O_4-Fe_2O_3 buffer conditions (Fig. 2). Laser ablation analyses of the glass between the cassiterite crystals yielded a Sn concentration near 85 ppm by weight. This number likely represents the cassiterite solubility in the silicate melt under run conditions. In Fig. 9, we compare this result with the cassiterite solubility data and model by Linnen et al. (1995, 1996). In this diagram, most solubility data follow slope of − 0.5, as expected from the reaction SnO_2 (cassiterite) = SnO (melt) + ½ O_2. Linnen et al. (1995, 1996) proposed that at high oxygen fugacity, the slope of the curve must become horizontal, once Sn^{4+} is the prevailing oxidation state in the melt, since then the dissolution may be described by the reaction SnO_2 (cassiterite) = SnO_2 (melt), which obviously is independent of oxygen fugacity. From a theoretical point of view, such a change to a horizontal slope indeed has to occur, but our data (Fig. 9) suggest that it occurs at much more oxidized conditions and, consequently, at much lower bulk Sn concentrations than originally proposed by Linnen et al. (1995, 1996). The likely explanation for this discrepancy is that in the studies Linnen et al. (1995, 1996), Sn concentration profiles were measured in quenched glasses near cassiterite crystals by electron microprobe. These profiles were used to extract diffusion coefficients and equilibrium solubilities in the glasses near the cassiterite surface. Very likely, the real Sn concentrations in the oxidized samples were below detection limit of the electron microprobe. Moreover, near the cassiterite surface, secondary fluorescence may perhaps have affected the measurements. We therefore propose that cassiterite solubility in granitic melts is likely described by the slightly modified version of the diagram introduced by Linnen et al. (1995, 1996) as shown in Fig. 9.

4.2. *Cassiterite solubility and the oxygen fugacity of magmatic-hydrothermal Sn deposits*

The data on cassiterite solubility in granitic melts by Linnen et al. (1995, 1996) can be combined with the fluid/melt partition coefficients obtained in the current study in order to predict cassiterite saturation in the coexisting fluid. The cassiterite solubility in the fluid is then simply obtained by multiplying the solubility in the melt with $D^{fluid/melt}$. This approach is reliable, as long as there is no major concentration dependence of $D^{fluid/melt}$. Neither in the current study nor in that of Zhao et al. (2022) any evidence was seen for such an effect and considering the generally low Sn concentrations involved, major deviations from Henry law are unlikely. Predicted Sn concentrations in fluid and granitic melt in equilibrium with cassiterite for various oxygen fugacities at 800–850 °C and 150–200 MPa are shown in Fig. 10. Cassiterite solubilities in granitic melts (black lines in Fig. 10) are mainly based on the work of Linnen et al. (1995, 1996), with the notable exception that in the light of our own data, we assume that the solubility curve with slope of 0.5 in Fig. 9 continues downwards to about 4 log units in fO_2 below QFM and only then turns into a horizontal line. Predicted cassiterite solubilities in the coexisting aqueous fluid are shown as red curves in Fig. 10 as a function of salinity. These data were obtained by multiplying the solubilities in the melt with $D^{fluid/melt}$ from this study, as described by the regression equations with parameters in Table 5. The experimental conditions of the current study (800 °C, 150 MPa) are slightly different from those of Linnen et al., (1995, 1996; 850 °C and 200 MPa), but it appears unlikely that this would introduce any major error.

In Fig. 10, predicted cassiterite solubilities are compared with measured Sn concentrations in low-salinity (≤ 15. wt.% NaCleq) fluid inclusions from the Zinnwald deposit (Erzgebirge, Germany; Korges et al., 2018). This is probably the most extensive data set for Sn concentrations in low-salinity fluids from magmatic-hydrothermal tin deposits. Data from some other deposits as compiled by Audétat (2019) overlap with the range of Sn concentrations reported for Zinnwald. Inspection of Fig. 10 shows that many of the Sn concentrations would not be stable under oxidizing conditions near the Fe_3O_4-Fe_2O_3 buffer, as the fluids would be oversaturated with cassiterite. At the Re-ReO_2 buffer, still about 20 % of the inclusions studied contains Sn concentrations above cassiterite saturation. In order to stabilize the highest Sn concentrations, the fluids must have been near the Ni-NiO buffer or even more reduced. It should be noted that the comparison of measured Sn concentrations in fluid inclusions with the curves in Fig. 10 can only give an upper limit of oxygen fugacity. Moreover, the fluid inclusions were trapped at temperatures significantly below 800 °C. As cassiterite solubility is expected to decrease with decreasing temperature (e.g. Wilson and Eugster, 1990), even more reducing conditions are required to stabilize the high Sn concentrations observed in many of the Zinnwald inclusions. Overall, the data agree with conclusions from previous field observations (e.g., Lehmann 1990, 2021) that the mobilization of tin in

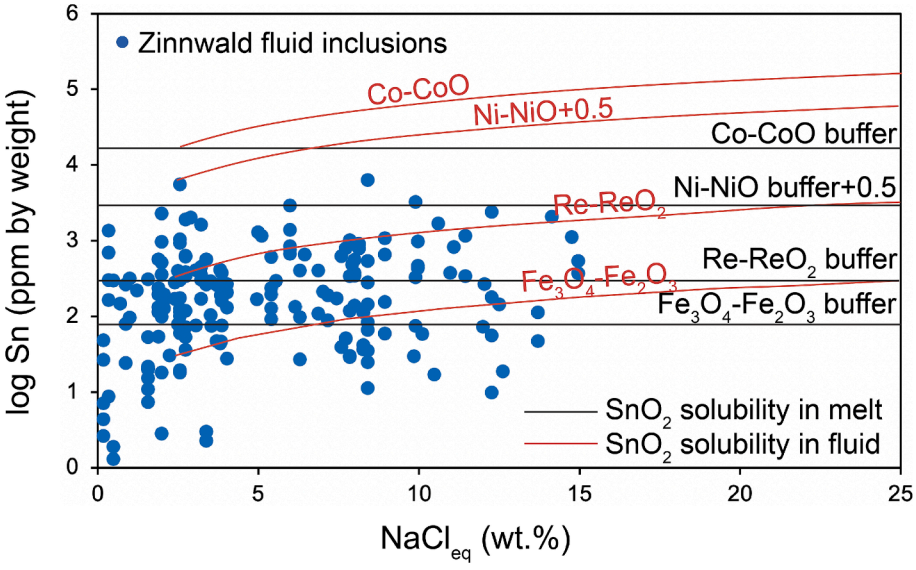

Fig. 10. Predicted cassiterite solubility in silicate melts and in coexisting fluids at 800–850 °C, 150–200 MPa and various oxygen fugacities, compared with Sn contents in fluid inclusions from the Zinnwald deposit (Erzgebirge, Germany; Korges et al. 2018). Black lines show Sn contents in the melt in equilibrium with cassiterite, red curves show the corresponding Sn concentrations in the fluid. Comparison with the fluid inclusion data indicates that the high Sn concentrations observed in some of them could not have been achieved under the oxidizing conditions of the Fe_3O_4-Fe_2O_3 or Re-ReO_2 buffers.

magmatic-hydrothermal systems requires reducing conditions that stabilize Sn^{2+}.

4.3. The formation of magmatic-hydrothermal Sn deposits

The formation of magmatic-hydrothermal tin deposits has remained rather controversial. Partially, this was due to early experimental studies that seemed to suggest that an efficient extraction of Sn into fluids is not possible (Nekrasov et al., 1990; Keppler and Wyllie, 1991; see also Schmidt et al., 2020). Moreover, the field relations in magmatic tin deposits do not always allow to clearly separate ore formation by fluids and by volatile-rich, highly-fractionated late-stage granitic melts. The high Sn concentrations in such melts (up to > 2000 ppm Sn, Webster et al., 1997) could perhaps lead to direct precipitation of cassiterite. In particular for greisen-type mineralization within the granite stocks (e.g. Lehmann, 1990, 2021), the relative importance of magmatic and hydrothermal processes for tin enrichment is hard to asses. In most magmatic-hydrothermal tin deposits, however, fluid inclusion and field evidence suggest precipitation of cassiterite from an aqueous fluid (e.g., Heinrich, 1990; Lehmann, 1990, 2021).

The new experimental data by Zhao et al. (2022) and those of the current study suggest that a mobilization of Sn by magmatic hydrothermal fluids is in principle possible. However, under most circumstances, the process may not be very effective. Fractional crystallization under reducing conditions, when Sn is incompatible in minerals (Wei et al., 2024), is likely the main mechanism for the concentration of Sn to economic grade deposits. Zhao et al. (2022) modelled Sn extraction by fluids during the Rayleigh-type fractional crystallization of a mildly peraluminous melt containing initially 2 or 5 wt% H_2O and 2000 ppm of Cl, assuming continuous fluid loss. The total extraction efficiency for Sn is only between 20 and 30 % for a mildly peraluminous melt at 99 % crystallization. Moreover, the largest contribution comes from the last aliquots of fluid released from the almost completely crystallized magma. How efficient this fluid release is at such high degrees of crystallization, however, is questionable. Numerical models suggest that fluid release from crystalizing granitic magmas is most efficient when the system is still in a partially convective stage and degassing rates decrease towards the end of crystallization (Lamy-Chappuis et al., 2020, Gruzdeva et al., 2024). Higher Sn extraction efficiencies can be reached in more strongly peraluminous systems (Zhao et al., 2022), but such high aluminum saturation indices are not reached in many Sn mineralized systems (e.g., Korges et al., 2018; Ni et al., 2023), although they do sometimes occur (e.g., Lehmann, 1990; Yuan et al., 2019). One of the expectations at the beginning of the current study was that maybe under conditions more reducing than the Ni-NiO buffer, $D^{fluid/melt}$ of Sn increases further, such that the extraction of Sn out of the magma becomes more efficient. The experimental data, however, do not support this and rather suggest a decrease of the fluid/melt partition coefficient.

According to all available experimental data, the availability of Cl is absolutely critical for the mobilization of Sn. In the absence of Cl, Sn likely does not significantly partition into an aqueous fluid, not even in the presence of fluorine (Duc-Tin et al., 2007). However, even in the presence of Cl, $D_{Sn}^{fluid/melt}$ will remain far below 25 for plausible salinities, such that Sn will usually continue to be enriched in the residual melt during fractional crystallization (e.g., Audétat, 2019), even if some loss of Sn to the fluid occurs. Therefore, high Sn concentrations will only be reached in the melt once most of the water and a considerable fraction of the Cl has already been released.

When discussing the behavior of Cl – and of Sn associated with Cl – in magmatic-hydrothermal systems, it is important to realize that the fluid/melt partition coefficient of Cl does not only increase with pressure, but it may also vary by more than one order of magnitude at constant P and T as a function of bulk Cl concentration (Webster, 1992; Kravchuk and Keppler, 1994; Hsu et al., 2019). For example, Kravchuk and Keppler (1994) observed a $D^{fluid/melt}$ of Cl of 21.5 for a dilute aqueous fluid, while for a concentrated saline brine, the same partition coefficient of Cl reached a value of 714 in the haplogranite-NaCl-KCl-H_2O system at otherwise identical conditions of 800 °C and 200 MPa. This concentration dependence of the Cl partition coefficient is due to the strong non-ideality of the NaCl-H_2O system at low pressures. A consequence of this effect can be that upon volatile saturation of a granitic magma, $D^{fluid/melt}$ of Cl may initially be very high and then decrease, as the fractionating melt is depleted in Cl. Whether such an effect occurs, depends on the pressure, bulk composition of the melt, and initial Cl concentration before fluid saturation. It is particularly likely for melts with an ASI near 1 and high initial Cl concentrations near 2000 ppm (Webster, 1992; Kravchuk and Keppler, 1994; Hsu et al., 2019). A strong initial depletion of Cl would then further reduce the efficiency of Sn extraction out of the melt into the fluid.

Volatile exsolution in a highly fractionated granitic magma may not only be induced by prolonged fractional crystallization, but also by a sudden release of fluid pressure. This may happen when fluid released by crystallization causes a temporary overpressure in the system, which causes fracturing of the surrounding rock. If these fractures extend to near the surface, and if the surrounding rock behaves like a stiff, brittle material, the pressure inside the factures will be hydrostatic, i.e., it will be generated by the fluid column inside the fracture. Since the fluid is by about a factor of three less dense than the surrounding rock, fluid pressure may also drop by the same factor for fractures extending to near the surface. Even if fractures do not extend all the way to the surface, this process may cause a sudden drop of fluid pressure from lithostatic pressure to some value between hydrostatic and lithostatic pressure. A consequence of this would be a rapid exsolution of a large amount of fluid, followed by relatively fast crystallization due to the increased liquidus and solidus temperatures. The rate of crystallization may be buffered by the associated heat release; however, fluid exsolution also efficiently removes heat from the system and as many tin deposits are related to rather small, highly differentiated intrusive bodies, conductive heat transport may also be relatively efficient. Evidence for such processes is seen in many magmatic-hydrothermal Sn deposits. Korges et al. (2018) showed detailed fluid inclusion evidence for such a depressurization event in the Zinnwald deposit. Moreover, many tin deposits worldwide show a combination of greisen-type mineralization of the granite body itself combined with vein fillings of fractures that emanate from the magma body (e.g. Lehmann, 1990, 2021; Ni et al., 2023). Further evidence for sudden pressure release is in the megacrystic microgranite texture of evolved granitic subintrusions, where a coarse-grained phenocryst assemblage of quartz-feldspar-biotite is set in a fine-grained matrix of the same mineralogical composition. Such “two-phase granites” likely developed from freezing on fluid release (Cobbing et al., 1986; see also Fig. 87 in Lehmann, 1990).

Table 6
Tin mobilization in a magmatic-hydrothermal system during rapid decompression caused by fracturing.

	D_{Cl}	$NaCl_{eq}$ (wt. %) in fluid	D_{Sn}	Sn (ppm) in fluid	% Sn extracted
Stage 1 Decompression 250 MPa − > 150 MPa	18	4.73	4.11	157	6
Stage 2 70 % crystallization due to decompression	19	5.17	4.49	375	32

D_{Cl} and D_{Sn} are the fluid/melt partition coefficients of Cl and Sn, respectively; % Sn extracted is the percentage of the total Sn content originally contained in the system that is extracted into the fluid at the individual step. Initial Sn and Cl contents in the melt are 40 and 2000 ppm, respectively. Water content drops from 6.5 to 5 wt% upon decompression. Temperature was assumed to be near 800 °C. In the second stage, 70 % crystallization releases 3.5 wt% of water as aqueous fluid.

In Table 6, we discuss the behavior of tin during a de-pressurization event related to fracturing of an evolving magmatic-hydrothermal system. We assume that upon exsolution of some fluid, fluid pressure drops rapidly from 250 to 150 MPa. According to the data of Holtz et al. (1995) for water solubility in haplogranitic magmas, this implies that the water content in the melt drops from 6.5 to 5 wt%, while at the same time, the solidus temperature increases from about 670 to 700 °C (Tuttle and Bowen, 1958; Keppler, 1989). This drop appears small, but if the melt was already close to the solidus, it may trigger extensive crystallization. At lower initial pressure, this effect would be even stronger; a pressure drop from 150 MPa to 55 MPa would raise the solidus by 70 °C. We assume that in such a situation, crystallization proceeds rather rapidly, possibly within weeks or months and the fluid released can be modelled by batch equilibrium in the system. Batch equilibrium is also assumed to describe the behavior of Sn during the initial depressurization step.

In the example illustrated in Table 6, we assume an initial granitic melt with 6.5 wt% water, 2000 ppm Cl, and 40 ppm Sn. The latter number is the lower limit of Sn concentrations from melt inclusions in evolved Sn-bearing granites in SE China (Ni et al., 2023). For the Cl partition coefficient, we use the model by Hsu et al. (2019), the Sn partition coefficient is from this study, with the regression coefficient for conditions close to Ni-NiO in Table 5. As Table 6 shows, the initial pressure release mobilizes only 6 % of the entire tin budget, but the successive crystallization of 70 % of the magma, which releases 3.5 wt% of dissolved water as fluid, transfers another 32 % of the initial tin budget to the fluid. Notably, this happens when the granite is still more than 30 % molten, such that an efficient release of fluids is possible. This situation is quite different from a fractional crystallization model with continuous fluid release, where most of the tin is only mobilized when the melt is mostly crystallized (see Zhao et al., 2022). Using our partitioning data, we calculated that during continuous fluid release driven by fractional crystallization at 150 or 200 MPa, only 26 % of the tin would be mobilized in the fluid, similar to the results of Zhao et al. (2022) and in contrast to the 38 % total tin extraction efficiency in the decompression model. We therefore suggest that de-pressurization due to fracturing and subsequent crystallization induced by water-loss may be a particularly efficient mechanism for the formation of hydrothermal tin deposits.

Both the numerical models presented here and those of Zhao et al. (2022) agree that even in circumstances that are favorable for the extraction of tin into the fluid, a large part of the initial tin budget will remain in the magma until the very last stages of fractional crystallization. According to the recent study of Wei et al. (2024) tin will be incompatible in minerals at strongly reducing conditions and may become enriched in residual melts up to the 2000 ppm level (Webster et al., 1997). The greisen-type mineralization seen in many magmatic-hydrothermal tin deposits may be related to the final stages of crystallization and degassing of such highly fractionated melts. The greisen alteration may have been caused by late-released fluids that did not travel very far away from the crystallizing magma. Fluids may have been involved in the formation of cassiterite, but without transporting the tin far away from the magmatic source. In the decompression model outlined above, the greisen-style mineralization may then actually be a late-stage event postdating the tin mineralization in veins. The assumption that much Sn remains in the melt phase on fractional crystallization/decompression is also supported by the fact that tin granites are characterized by elevated Sn contents as expressed in systematic magmatic tin enrichment trends (e.g., Lehmann, 1990). This is different to Cu porphyries where Cu partitions quantitatively into the saline aqueous fluid phase (e.g., Keppler and Wyllie, 1991).

5. Conclusions

(1) The fluid/melt partition coefficient of Sn increases linearly with the Cl concentration in the fluid. A maximum of $D^{fluid/melt}$ is reached near the Ni-NiO buffer, while the partition coefficient decreases both toward more oxidizing and towards more reducing conditions.

(2) Strongly reducing conditions may be favorable for the formation of Sn deposits mainly because they increase SnO_2 solubility in the melt and therefore allow Sn enrichment during fractional crystallization. Our data suggest that SnO_2 solubility under oxidizing conditions near the Fe_3O_4-Fe_2O_3 buffer is even much lower than previously thought. We show that under such oxidizing conditions, the formation of Sn deposits is impossible, as cassiterite saturation in fluid and melt would already occur at low Sn concentrations.

(3) Even under optimum conditions, the mobilization of Sn into fluids is not very efficient and some cassiterite in magmatic-hydrothermal Sn deposits may have directly precipitated from late-stage, volatile-rich melts or from fluids that did not travel far away from the magmatic source.

(4) Fluid release driven by slow fractional crystallization is not very efficient in mobilizing Sn in fluids, as Cl is lost to the fluid before Sn is strongly enriched in the residual melt. A more efficient mechanism to extract Sn may be a sudden pressure drop induced by fracturing and subsequent rapid crystallization. In such a scenario, Cl may still be abundant in the system once high Sn concentrations are reached in residual melts.

CRediT authorship contribution statement

Hans Keppler: Writing – original draft, Visualization, Validation, Methodology, Investigation, Funding acquisition, Formal analysis, Conceptualization. **Andreas Audétat:** Writing – review & editing, Validation, Investigation.

Data availability

Data are available through Figshare, https://doi.org/10.6084/m9.figshare.26968807.

Declaration of competing interest

The authors declare that they have no known competing financial interests or personal relationships that could have appeared to influence the work reported in this paper.

Acknowledgements

We thank Raphael Njul for sample polishing and Detlef Krauße for electron microprobe analyses. Constructive reviews by Bernd Lehmann, Zoltan Zajacz and by an anonymous referee helped to improve the manuscript. This work was supported by the priority program DOME of German Science Foundation (DFG; Ke 501/16-1).

Appendix A. Supplementary material

Supplementary Table S1 contains the analyses of all fluid inclusions and adjacent glass phases measured in this study. Supplementary material to this article can be found online at https://doi.org/10.1016/j.gca.2025.02.007.

References

Audétat, A., 2019. The metal content of magmatic-hydrothermal fluids and its relationship to mineralization potential. Econ. Geol. 114, 1033–1056.
Bhalla, P., Holtz, F., Linnen, R.L., Behrens, H., 2005. Solubility of cassiterite in evolved granitic melts: effect of T, fO_2, and additional volatiles. Lithos 80, 387–400.
Breiter, K., 2012. Nearly contemporaneous evolution of the A- and S-type fractionated granites in the Krušné hory / Erzgebirge Mts., Central Europe. Lithos 151, 105–121.
Cobbing, E.J., Mallick, D.I.J., Pitfield, P.E.J., Teoh, L.H., 1986. The granites of the Southeast-Asian tin belt. J. Geol. Soc. 143, 537–550.

Duc-Tin, Q., Audetat, A., Keppler, H., 2007. Solubility of tin in (Cl, F)-bearing aqueous fluids at 700 ℃, 140 MPa: A LA-ICP-MS study on synthetic fluid inclusions. Geochim. Cosmochim. Acta 71, 3323–3335.
Fang, J., Chou, I.M., Audétat, A., Zhang, L., 2024. Quantitative redox measurements for hydrothermal experiments conducted in cold-seal pressure vessels. Chem. Geol. 663, 122286.
Farges, F., Linnen, R.L., Brown, G.E., 2006. Redox and speciation of tin in hydrous silicate glasses: A comparison with Nb, Ta, Mo and W. Canadian Mineral. 44, 795–810.
Gruzdeva, Y., Weis, P., Andersen, C., 2024. Timing of volatile degassing from hydrous upper-crustal magma reservoirs with implications for porphyry copper deposits. J. Geophys. Res. Solid Earth 129, e2023JB028433.
Heinrich, C.A., 1990. The chemistry of hydrothermal tin (-tungsten) ore deposition. Econ. Geol. 85, 457–481.
Holtz, F., Behrens, H., Dingwell, D.B., Johannes, W., 1995. H_2O solubility in haplogranitic melts: Compositional, pressure, and temperature dependence. Am. Mineral. 80, 94–108.
Hu, X., Bi, X., Hu, R., Shang, L., Fan, W., 2008. Experimental study on tin partitioning between granitic silicate melt and coexisting aqueous fluid. Geochem. J. 42, 141–150.
Huebner, J.S., 1973. Buffering techniques for hydrostatic systems at elevated pressures. In: Ulmer, G.C. (Ed.), Research Techniques for High Pressure and High Temperature. Springer, New York, pp. 123–177.
Hsu, Y.J., Zajacz, Z., Ulmer, P., Heinrich, C.A., 2019. Chlorine partitioning between granitic melt and H_2O-CO_2-NaCl fluids in the Earth's upper crust and implications for magmatic-hydrothermal ore genesis. Geochim. Cosmochim. Acta 261, 171–190.
Ishihara, S., 1977. The magnetite series and ilmenite series granitic rocks. Mining Geol. 27, 293–305.
Ishihara, S., 1981. The granitoid series and mineralization. In: Econ. Geol. 75th Anniv. Volume, pp. 458–484.
Jochum, K.P., Weis, U., Stoll, B., Kuzmin, D., Yang, Q.C., Raczek, I., Jacob, D.E., Stracke, A., Birbaum, K., Frick, D.A., Gunther, D., Enzweiler, J., 2011. Determination of reference values for NIST SRM 610-617 glasses following ISO guidelines. Geostand. Geoanal. Res. 35, 397–429.
Keppler, H., 1989. The influence of the fluid phase composition on the solidus temperatures in the haplogranite system $NaAlSi_3O_8$-$KAlSi_3O_8$-SiO_2-H_2O-CO_2. Contrib. Mineral. Petrol. 102, 321–327.
Keppler, H., 2010. The distribution of sulfur between haplogranitic melts and aqueous fluids. Geochim. Cosmochim. Acta 74, 645–660.
Keppler, H., Wyllie, P.J., 1991. Partitioning of Cu, Sn, Mo, W, U, and Th between melt and aqueous fluid in the systems haplogranite-H_2O-HCl and haplogranite-H_2O-HF. Contrib. Mineral. Petrol. 109, 139–150.
Korges, M., Weis, P., Lüders, V., Laurent, O., 2018. Depressurization and boiling of a single magmatic fluid as a mechanism for tin-tungsten deposit formation. Geology 46, 75–78.
Kravchuk, I., Keppler, H., 1994. Distribution of chloride between aqueous fluids and felsic melts at 2 kbar and 800 ℃. Eur. J. Mineral. 6, 913–923.
Lamy-Chappuis, B., Heinrich, C.A., Driesner, T., Weis, P., 2020. Mechanisms and patterns of magmatic fluid transport in cooling hydrous intrusions. Earth Planet. Sci. Lett. 535, 116111.
Launay, G., Sizaret, S., Guillou-Frottier, L., Fauguerolles, C., Champallier, R., Gloaguen, E., 2019. Dynamic permeability related to greisenization reactions in Sn-W ore deposits: Quantitative petrophysical and experimental evidence. Geofluids 2019, Article ID 5976545.
Lehmann, B., 1982. Metallogeny of tin: magmatic differentiation versus geochemical heritage. Econ. Geol. 77, 50–59.
Lehmann, B., 1990. Metallogeny of Tin. In: Lecture Notes in Earth Sciences, 32. Springer, Berlin.
Lehmann, B., 2021. Formation of tin ore deposits: A reassessment. Lithos 402–403, 105756.
Linnen, R.L., Pichavant, M., Holtz, F., Burgess, S., 1995. The effect of fO_2 on the solubility, diffusion, and speciation of tin in haplogranitic melt at 850 ℃ and 2 kbar. Geochim. Cosmochim. Acta 59, 579–1588.
Linnen, R.L., Pichavant, M., Holtz, F., 1996. The combined effects of fO_2 and melt composition on SnO_2 solubility and tin diffusivity in haplogranitic melts. Geochim. Cosmochim. Acta 60, 4965–4976.
Nekrasov, I.Y., Epel'baum, M.B., Sobolev, V., 1980. Partitioning of tin between melt and chloride fluid in the granite–SnO–SnO_2 fluid system. Dokl. Acad. Sci. USSR, Earth Sci. Section 252, 165–168.
Ni, P., Pan, J.Y., Han, L., Cui, J.M., Gao, Y., Fan, M.S., Li, W.S., Chi, Z., Zhang, K.H., Cheng, Z.L., Liu, Y.P., 2023. Tungsten and tin deposits in South China: Temporal and spatial distribution, metallogenic models and prospecting directions. Ore Geology Reviews 157, 105453.
Pollard, P.J., Pichavant, M., Charoy, B., 1987. Contrasting evolution of fluorine- and boron-rich tin systems. Mineralium Deposita 22, 315–321.
Robie, R.A., Hemingway, B.S., 1995. Thermodynamic properties of minerals and related substances at 298.15 K and 1 bar (10^5 Pascals) pressure and at higher temperatures. US Geolog. Surv. Bull. 2131, 1–461.
Romer, R.L., Kroner, U., 2016. Phanerozoic tin and tungsten mineralization-tectonic controls on the distribution of enriched protoliths and heat sources for crustal melting. Gondwana Res. 31, 60–95.
Schmidt, C., Romer, R.L., Wohlgemuth-Ueberwasser, C.C., Appelt, O., 2020. Partitioning of Sn and W between granitic melt and aqueous fluid. Ore Geology Rev. 117, 103263.
Schwartz, M.O., Rajah, S.S., Askury, A.K., Putthapiban, P., 1995. The Southeast-Asian tin belt. Earth Sci. Rev. 38, 95–286.
Simons, B., Andersen, J.C.Ø., Shail, R.K., Jenner, F.E., 2017. Fractionation of Li, Be, Ga, Nb, Ta, In, Sn, Sb, W and Bi in the peraluminous Early Permian Variscan granites of the Cornubian Batholith: Precursor processes to magmatic-hydrothermal mineralization. Lithos 278–281, 491–512.
Tuttle, O.F., Bowen, N.L., 1958. Origin of granites in the light of experimental studies in the system $NaAlSi_3O_8$-$KAlSi_3O_8$-SiO_2-H_2O. Geol. Soc. Am. Mem. 74, 1–153.
Webster, J.D., Thomas, R., Rhede, D., Forster, H.J., Seltmann, R., 1997. Melt inclusions in quartz from an evolved peraluminous pegmatite: Geochemical evidence for strong tin enrichment in fluorine-rich and phosphorus-rich residual liquids. Geochim. Cosmochim. Acta 61, 2589–2604.
Webster, J.D., 1992. Fluid-melt interactions involving Cl-rich granites. Experimental study from 2 to 8 Kb. Geochim. Cosmochim. Acta 56, 659–678.
Wei, C.X., Xiong, X., Wang, J., Huang, F., Gao, M., 2024. Partitioning of tin between mafic minerals, Fe-Ti oxides and silicate melts: Implications for tin enrichment in magmatic processes. Geochim. Cosmochim. Acta 372, 81–100.
Wilson, G.A., Eugster, H.P., 1990. Cassiterite solubility and tin speciation in supercritical chloride solutions. Geochemical Society Special Publication 2 (Fluid Mineral Interactions: A Tribute to H.P. Eugster), 179-195.
Wolf, M., Romer, R.L., Franz, L., Lopez-Moro, F.J., 2018. Tin in granitic melts: The role of melting temperature and protolith composition. Lithos 310, 20–30.
Wu, S., Audétat, A., Jochum, K.P., Wang, H., Chen, J., Stoll, B., Zhang, C., Bao, Z., Yang, S.-Y., Li, C., Wang, X., Xu, C., Xu, L., Huang, C., Xie, L., Yang, Y.-H., Yang, J., 2022. Three natural andesitic to rhyolitic glasses (OJY-1, OH-1, OA-1) as reference materials for in-situ microanalysis. Geostand. Geoanal. Res.
Yuan, S., Williams-Jones, A.E., Romer, R.L., Zhao, P., Mao, J., 2019. Protolith-related thermal controls on the decoupling of Sn and W in Sn-W metallogenic provinces: Insights from the Nanling region, China. Econ. Geol. 114, 1005–1012.
Zhao, P., Zajacz, Z., Tsay, Z., Yuan, S., 2022. Magmatic-hydrothermal tin deposits form in response to efficient tin extraction upon magma degassing. Geochim. Cosmochim. Acta 316, 331–346.